atmosphere

MDPI

Article

Amine-Modified Biochar for the Efficient Adsorption of Carbon Dioxide in Flue Gas

Wengang Tian [1], Yanxia Wang [2], Jian Hao [1], Tuo Guo [3], Xia Wang [4], Xiaoju Xiang [1] and Qingjie Guo [1,*]

[1] State Key Laboratory of High–Efficiency Utilization of Coal and Green Chemical Engineering, Ningxia University, Yinchuan 750021, China; wengangtian@stu.nxu.edu.cn (W.T.); haojian@nxu.edu.cn (J.H.); xiangxiaoju@stu.nux.edu.cn (X.X.)
[2] Department of Chemistry and Chemical Engineering, North Minzu University, Yinchuan 750021, China; 2021007@nmu.edu.cn
[3] Department of Chemistry, University College London, London WC1H 0AJ, UK; tuo.guo.20@ucl.ac.uk
[4] Department of Chemistry and Chemical Engineering, Weifang University, Weifang 261061, China; 20160012@wfu.edu.cn
* Correspondence: qjguo@qust.edu.cn; Tel.: +86-951-206-2835

Abstract: Biochar-based carbonaceous adsorbents are gaining interest due to their high availability, ease of modification, and low cost; however, they show limited adsorption of CO_2 in flue gas due to common textural properties. In this study, TEPA-modified biochar was used to prepare a solid amine adsorbent for the efficient capture of CO_2 in flue gas. First, the porous biochar was prepared with $FeCl_3$, $Mg(NO_3)_2$, and H_2O (g) as activators and walnut shells as carbon sources. Next, the biochar was modified with TEPA to obtain a solid amine adsorbent. Porous texture properties and sample surface functional groups were characterized, and we measured the adsorption CO_2 of the amine-modified biochar in a breakthrough adsorption device. Results showed that biochar has a large specific surface area (744.38 m^2 g^{-1}), a total pore volume of 1.41 cm^3 g^{-1}, and a high mesoporous volume ratio (82.7%). The high pore volume provided a more efficient support space for loading tetraethylenepentamine (TEPA). The adsorbent had an excellent CO_2 adsorption capacity, corresponding to 2.82 mmol g^{-1}, which increased to 3.31 mmol g^{-1} and kept water resistance at 10% H_2O (g) simulated flue gas (SFG). The FTIR analysis showed that H_2O (g) inhibited urea production after cyclic adsorption. Therefore, solid amine adsorbent created by amine-modified biochar has potential advantages in its application for capturing CO_2 in SFG.

Keywords: walnut shell; biochar; coactivation; adsorbent; CO_2 adsorption

check for updates

Citation: Tian, W.; Wang, Y.; Hao, J.; Guo, T.; Wang, X.; Xiang, X.; Guo, Q. Amine-Modified Biochar for the Efficient Adsorption of Carbon Dioxide in Flue Gas. *Atmosphere* **2022**, *13*, 579. https://doi.org/10.3390/atmos13040579

Academic Editor: Marcelo I. Guzman

Received: 22 February 2022
Accepted: 31 March 2022
Published: 4 April 2022

Publisher's Note: MDPI stays neutral with regard to jurisdictional claims in published maps and institutional affiliations.

Copyright: © 2022 by the authors. Licensee MDPI, Basel, Switzerland. This article is an open access article distributed under the terms and conditions of the Creative Commons Attribution (CC BY) license (https://creativecommons.org/licenses/by/4.0/).

1. Introduction

CO_2 emissions caused by fossil energy are important causes of global warming and the greenhouse effect [1]. Adsorption is the most promising method for reducing CO_2 emissions from SFG because of its low corrosiveness and low energy consumption. At the same time, it does not require significant modifications to the considerable existing equipment [2–4]. The excellent adsorbent is the core of efficient CO_2 adsorption. Solid amine adsorbents remove CO_2 from SFG because of their multiple active sites, high adsorption capacity, broad application temperature range, and eco-friendliness [5–8]. The carrier is the core and essential for synthesizing the solid amine adsorbent. Commonly, carriers can be divided into noncarbon and carbon materials [7]. Noncarbon carriers include alkali-metal materials, metal oxides, metal–organic frameworks (MOFs), and molecular sieves [5–7]. Carbon material carriers include graphene oxide (GO), activated carbon fibers, carbon nanotubes, and ordered mesoporous carbon. Although these materials have excellent pore structure parameters, complex preparation methods and high production cost limit their large-scale production.

Compared with the abovementioned carriers, biochar has been extensively used in various fields because of its broad availability, low cost, well-strung pores, and ample surface

functional groups. Biochar has a large specific surface area (S_{BET}), total pore volume (V_T), and pore diameter (P_d); hence, it is suitable as a carrier. By introducing different functional groups, adsorbents with different functions can be easily obtained [4,9]. Nevertheless, biochar obtained using traditional methods has multiple limitations; hence, more studies have been conducted with the aim of improving the structure of biochar [10–12]. Usually, chemical and physical activation are employed to improve the structural properties of biochar, such as the S_{BET} and V_T. KOH [13], H_3PO_4 [14], K_2CO_3 [15], HNO_3 [16], O_2 [17], $ZnCl_2$ [18], $FeCl_3$ [19], $MgCl_2$ [20], and steam [21] had been used as activators to optimize the structure of biochar. Although the usage of KOH, NaOH, and other strong acid and alkali activators can yield a suitable S_{BET}, the pore diameter is generally small. Furthermore, the loading of organic amine leads to the plugging of these pores, which is not conducive to CO_2 diffusion and adsorption. Moreover, disposable activators (NaOH, H_3PO_4, K_2CO_3, HNO_3) are highly corrosive and difficult to recycle. Their large-scale application would cause considerable damage to the environment. H_2O (g) is considered to be an eco-friendly activator for creating new pores and expanding the pore diameter. However, if only H_2O (g) is used as the activator, it is difficult to control the activation rate and pore structure of biochar [22–24]. Furthermore, metal salts activation was used to prepare biochar. Using the metal salts as activating agents to prepare biochar accelerates the pyrolysis of biomass, promotes graphitization, and creates pores for biochar. Liu et al. [20] obtained mesoporous biochar with an S_{BET} of 421.4 $m^2\ g^{-1}$ using high-temperature activation and pyrolysis of $FeCl_3$ preloaded on the biomass surface. The coactivated biochar with two metal salts was more effective than the single metal salts biochar. Guo et al. [25] used $MgCl_2$ and $FeCl_3$ loading on the biomass surface and obtained biochar with S_{BET}, S_{meso}, and V_T of 664.55 $m^2\ g^{-1}$, 92.76 $m^2\ g^{-1}$, and 0.33 $cm^3\ g^{-1}$, respectively. Yan et al. [18] prepared porous biochar with $ZnCl_2$. S_{BET} and V_{micro} reached 852.41 $m^2\ g^{-1}$ and 0.086 $cm^3\ g^{-1}$, respectively. Metal salts are used as activators that could prepare biochar with more micropores. In addition, Idrees et al. [13] prepared biochar with high microporosity using KOH-activated peanut shells, and the adsorption capacity of CO_2 was 5.32, 4.24, and 1.21 mmol g^{-1} at 0, 25, 30 °C, P = 1 bar, respectively. Microporous biochar has been used for CO_2 adsorption at low temperatures and sewage treatment. However, the adsorption capacity of biochar for CO_2 in flue gas is lower, and there are few studies on the realization of efficient adsorption of CO_2 with biochar under high-temperature conditions. In order to achieve the effective adsorption of CO_2 in SFG, it is necessary to research biochar modification.

Walnuts of world production are over 3.7 million t, and China is the largest producer, with 1.06 million tons. After walnut kernels are used for food purposes, the shell remains as a by-product or waste, although walnut shell biomass is also a renewable source of raw material [26]. Walnut shell has a low ash content and a high-quality natural structure, which is conducive to the formation of a developed pore structure and is an excellent raw material for the preparation of biochar.

In this study, $FeCl_3$, $Mg(NO_3)_2$, and H_2O (g) simultaneously activated and pyrolyzed walnut shells to prepare more mesoporous biochar. Different proportions of TEPA modified biochar to obtain solid amine adsorbents; subsequently, biochar and the adsorbent's structural properties and thermal stability were characterized. The adsorption capacity and cycling stability of the adsorbents were measured under different SFG. Moreover, the adsorption and deactivation mechanisms of the adsorbents were examined.

2. Experimental Section

2.1. Materials

Walnut shells were obtained from a local market (Yinchuan, Ningxia, China); $FeCl_3{\cdot}6H_2O$ and $Mg(NO_3)_2{\cdot}6H_2O$ (AR) were purchased from Sigma-Aldrich (St. Louis, MO, USA); analytically pure HCl (AR, hydrochloric acid 36.0 wt.%) was obtained from Sinopharm Chemical Reagent; analytically pure absolute ethanol (AR, 99.7 wt.%) was obtained from Damao Chemical Reagent Factory, Tianjin, China; high-purity CO_2 and N_2,

(99.999%) were obtained from Ningxia Guangli Gas Co, Yinchuan, China. The elemental and industrial analyses of the walnut shells are shown in Table 1.

Table 1. Industrial analysis and elemental analysis of walnut shell.

Samples	Elemental Analysis (wt%, Ad)					Industrial Analysis (wt%, Ad)			
	C	H	O [a]	N	S	M	A	V	FC
Walnut shell	49.94	5.86	43.96	0.20	0.043	6.21	1.86	81.23	10.69

Note: [a] indicates the use of differential subtraction; Ad: air-dried basis. M: moisture; A: ash; V: volatile; FC: fixed-carbon.

2.2. Synthesis of the Amine-Functionalized Sorbent

2.2.1. Preparation of Biochar

First, walnut shells were rinsed with water and dried at 100 °C. Then, they were crushed and sieved to form 50–100 mesh-sized particles. $FeCl_3 \cdot 6H_2O$ (3 g) and $Mg(NO_3)_2 \cdot 6H_2O$ (6 g) were placed in 500 mL of deionized water and stirred until the solution was dispersed; 10 g of biomass as the carbon source was then added to the metal salts solution for impregnation, and the solution was then evaporated to dryness by stirring at 150 °C, and 400 r min^{-1}. In a tube furnace, one-step pyrolysis and carbonization were performed in an inert atmosphere (H_2O 0.1 mL min^{-1}, N_2 flow 200 mL min^{-1}) at 900 °C for 100 min. After carbonization, H_2O (g) was switched to pure N_2 and cooled to a low temperature. The carbonization biochar was washed with 0.3 M HCl for 6 h to remove the metal oxides and a small amount of ash and then repeatedly washed using distilled water to neutralize it. Finally, the biochar was obtained by drying. Samples were named RBC (without activation), HBC (H_2O (g) activated), FMBC ($FeCl_3$, and $Mg(NO_3)_2$ coactivated) and CBC ($FeCl_3$, $Mg(NO_3)_2$, and H_2O (g) coactivated).

2.2.2. Preparation of Amine-Functionalized Biochar

TEPA was uniformly dispersed in anhydrous ethanol after the addition of the CBC. The solution was stirred with a heating plate at 35 °C and 200 r min^{-1} until it was completely evaporated. Finally, samples were dried (80 °C dry for 10 h under vacuum) to obtain the TEPA-loaded adsorbent. Samples were named CBC-X-TEPA, where X (X = 20, 30, 40, 50, and 60) refers to the mass fraction of TEPA.

2.3. Characterization

The ultimate analysis of samples was characterized by the elemental analyzer (EA 3000, Euro Vector, Pavia, Italy). The textural properties of the samples were measured using the method of low-temperature N_2 adsorption–desorption with a rapid surface area and porosity analyzer (Autosorb-iQ, Quantachrome Instruments, Boynton Beach, FL, USA). The morphology features of samples were observed using scanning electron microscopy (SEM Quanta 400, FEI company, Hillsboro, OR, USA). The crystalline phase of samples was tested by X-ray diffractometer (XRD, Bruker, Germany) at Cu radiation, 40 kV, 40 mA, and 2θ range of 3°–85°. The samples graphitization was analyzed by Raman spectra (DXR2xi Raman, Thermo Fisher Scientific, Waltham, Massachusetts, U.S. wavelength range from 500 to 3500 cm^{-1}). The functional groups on the surface of the samples were analyzed by using FTIR (TENSOR II, Bruker, Germany). Thermogravimetric analysis (TGA STA449 F3, NETZSCH-Gerätebau GmbH, Selb, Germany) was employed to analyze the thermal stability of samples.

2.4. CO_2 Adsorption

CO_2 sorption on adsorbent was performed in a breakthrough adsorption setup that is shown in Figure 1. The adsorption column (with length 40 cm and inner diameter 1 cm) was filled with adsorbent 1 g. In SFG (15% CO_2/85% N_2), the sorption CO_2 capacity of adsorbent with different TEPA loaded was tested to select the best. Subsequently, CO_2 sorption of the best adsorbent was performed in SFG (15% CO_2/75% N_2/10% H_2O). The

specific steps of the adsorption experiment were as follows: N_2 (30 mL/min) was aerated in the adsorption bed, and the temperature was slowly heated to 105 °C and kept for 1 h. Then, the temperature of the adsorption bed was lowered to a constant temperature of 60 °C; the adsorption experiment was started by introducing SFG into the adsorption bed. When the outlet and inlet gases had the same CO_2 concentration, the experiment was stopped. For the recycle experiment, the absorbent was exposed to SFG (30 mL min^{-1}) at 60 °C to adsorb CO_2. When the adsorption reaction ended, the high-purity N_2 (30 mL min^{-1}) was aerated in the adsorption bed, and the temperature was heated to 105 °C and maintained for 1 h. The test was repeated ten times. The adsorption capacity of the adsorbent was calculated using the following equation:

$$q = \frac{1}{M} \times \left[\left(\int_0^t Q \times \frac{C_0 - C}{1 - C} \right) \right] \times \frac{T_0}{T} \times \frac{1}{V_m} \quad (1)$$

where q represents the adsorption capacity of CO_2, mmol g^{-1}; M is the quality of the CBC-X-TEPA, g; t is adsorption time, min. Q is the total SFG flow, cm^3 min^{-1}; C_0 and C are the input and output CO_2 concentrations; Vol.%; t is the adsorption time, min; T_0 represents absolute zero, 273 K; T is adsorption temperature, K; and V_m is the standard molar volume, 22.4 L mol^{-1}.

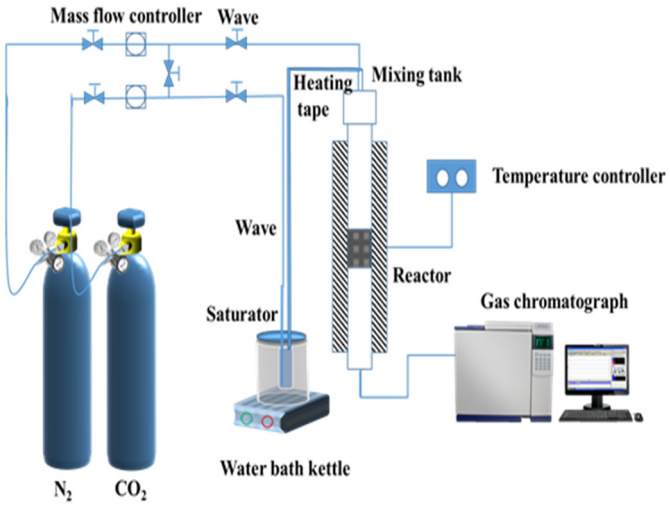


Figure 1. Schematic of CO_2 breakthrough adsorption setup.

Amine (TEPA) efficiency was employed to investigate the utilization efficiency of organic amine loaded into biochar and the adsorption capacity of the adsorbent for CO_2. The calculation formula of amine efficiency was as follows:

$$TEPA\ efficiency = \frac{nCO_2}{m_{amine}} \quad (2)$$

where nCO_2 is the saturated adsorption capacity of the adsorbent, mmol g^{-1}; m_{amine} refers to the quality of amine, g.

3. Results and Discussion

3.1. Biochar Preparation Mechanism

$FeCl_3$, $Mg(NO_3)_2$, and H_2O (g) played important roles in biomass pyrolysis. In the heating process, $FeCl_3 \cdot 6H_2O$ pyrolysis and gradual transformation into Fe_2O_3 and Fe_3O_4 are shown in Equations (3)–(6) [25]. Mg $(NO_3)_2 \cdot 6H_2O$ decomposed into MgO after dehydration in the pyrolysis reaction process. The reactions are shown in Equations (7) and (8) [24]. MgO and Fe_3O_4 formed the MgO and FeO solid solution during pyrolysis. H_2O (g) reacted with the surface carbon of biochar generated after biomass pyrolysis and then gradually

diffused into the internal pores of biochar as the reaction proceeded, and the reactions formulae of H_2O (g) and C are shown in Equations (9)–(11) [23].

The XRD patterns were employed to investigate the metal-conversion process during the preparation of biochar. The specific reaction is shown in Figure S1. During the initial 10 min pyrolysis stage, $FeCl_3 \cdot 6H_2O$ and $Mg(NO_3)_2 \cdot 6H_2O$ first pyrolyzed into Fe_2O_3/Fe_3O_4 and MgO. Fe_2O_3/Fe_3O_4 reduced to FeO and Fe as shown in Equations (12) and (13) [19,25], then they sintered and agglomerated as MgO(0.91)FeO(0.09). When the reaction proceeded to 20 min and 40 min, MgO(0.91)FeO(0.09) transformed into MgO(0.77)FeO(0.23). At 60 min, H_2O (g) introduction made the FeO of MgO(0.77)FeO(0.23) completely oxidize to Fe_3O_4; the reactions are shown in Equations (14) and (15) [27]. In addition, the sintered metal oxides separated from each other. The reaction mechanism is shown in Figure 2. Since the metal oxides were distributed on the biochar surface after pyrolysis, they could prevent the H_2O (g) from entering the pores and hence prevent it from overreacting and collapsing the internal pore. In addition, the carbon peak in the biochar gradually weakened, which is attributed to high temperatures forming a more disordered structure [22].

$$FeCl_3 \cdot 6H_2O \rightarrow FeCl_3 \cdot 3H_2O + 3H_2O \quad (3)$$

$$FeCl_3 \cdot 3H_2O \rightarrow Fe(OH)_3 + 3HCl \quad (4)$$

$$Fe(OH)_3 \rightarrow FeO(OH) \rightarrow Fe_2O_3 \quad (5)$$

$$3Fe_2O_3 + 4H_2(CO,\ C) \rightarrow 2Fe_3O_4 + 4H_2O(CO_2,\ CO) \quad (6)$$

$$Mg(NO_3)_2 \cdot 6H_2O \rightarrow Mg(NO_3)_2 + 6H_2O \quad (7)$$

$$Mg(NO_3)_2 \rightarrow MgO + 2NO_2 + \frac{1}{2}O_2 \quad (8)$$

$$3Fe + 4H_2O(g) \rightarrow Fe_3O_4 + 4H_2 \quad (9)$$

$$C + H_2O(g) \rightarrow CO + H_2 \quad (10)$$

$$CO + H_2O(g) \rightarrow CO_2 + H_2 \quad (11)$$

$$Fe_3O_4 + H_2(CO,\ C) \rightarrow 3FeO + H_2O(CO_2,\ CO) \quad (12)$$

$$Fe_3O_4 + 4H_2(CO,\ C) \rightarrow 3Fe + 4H_2O(CO_2,\ CO) \quad (13)$$

$$3FeO + H_2O(g) \rightarrow Fe_3O_4 + H_2 \quad (14)$$

$$CO_2 + C \rightarrow 2CO \quad (15)$$

3.2. Sample Characterization

The SEM characterization of samples was carried out to investigate the effect of the preparation method on the structure and morphology. Figure 3a shows the RBC without metal salts, and H_2O (g) activation exhibited macropores, with an undeveloped pore structure and no lamellar structure. Figure 3b shows results after being coactivated with metal salts and H_2O (g); the surface of CBC possessed distributed metal particles, which were produced by $FeCl_3$ and $Mg(NO_3)_2$. Figure 3c shows results after the removal of these metal particles. The CBC surface showed a stacked lamellar structure with multiple large pores, which was different from what was roughly observed with irregular crakes, plates, and particles reported by Guo et al. [25]. The large pores on the surface were partly produced by the spillage of the volatile fraction during thermal decomposition and partly formed by the removal of large-sized metal particles sintered on the biochar surface. Compared with RBC, the surface structure and morphology of the CBC had undergone tremendous changes, which showed that metal salts and H_2O (g) had a great influence on the formation of biochar. This could be more conducive to TEPA loading and CO_2 adsorption on the surface of biochar. Figure 3d is an SEM image of the adsorbent that shows the stacked lamellar structure and surface pores on the CBC did not change significantly after the TEPA

loading. The presence of pores of different sizes on the adsorbent surface could provide large passages, accelerating CO_2 diffusion into the internal part of the adsorbent.

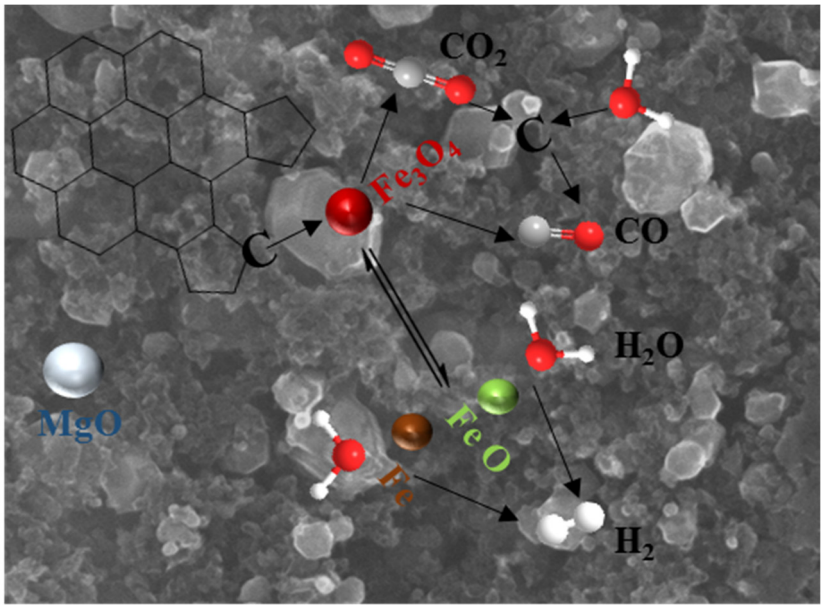


Figure 2. The biochar preparation mechanism.

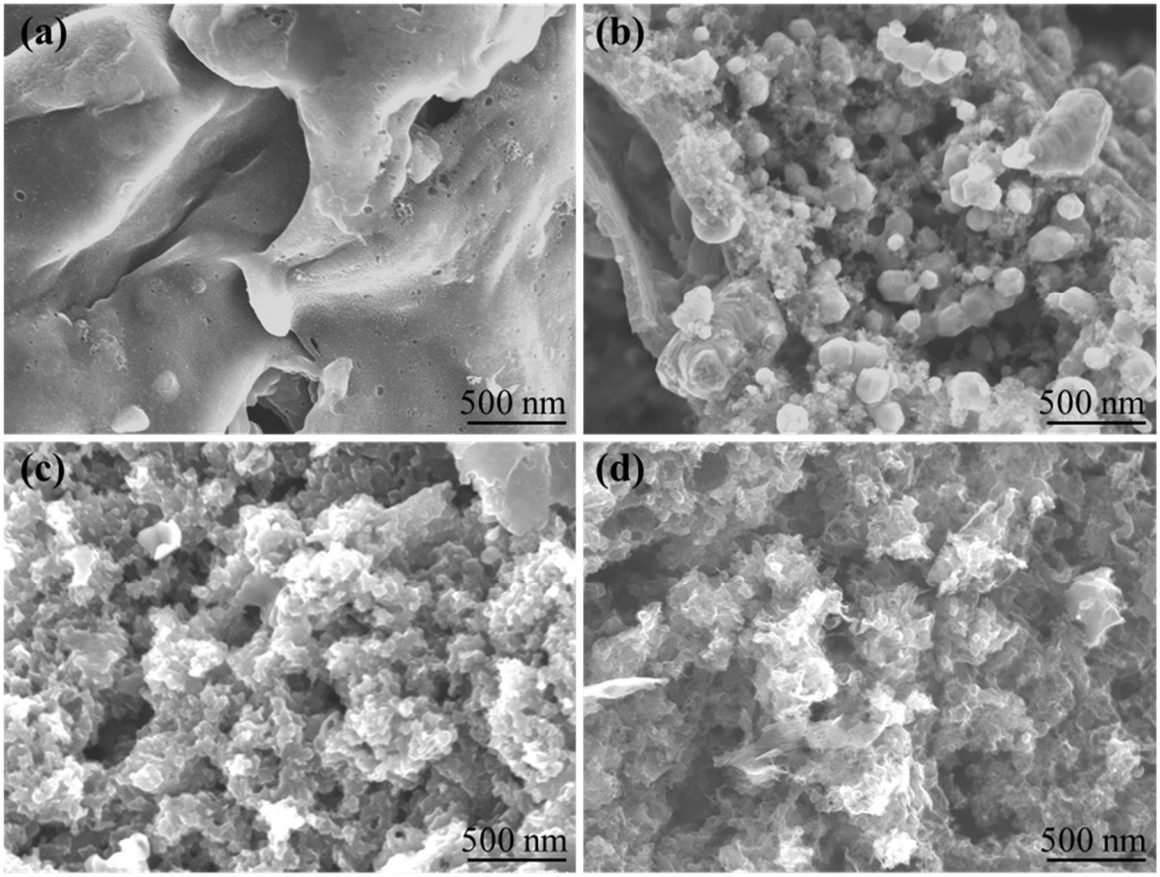


Figure 3. SEM images of (**a**) RBC, (**b**) CBC before removal of metal particles, (**c**) CBC after removal of metal particles, and (**d**) CBC-50-TEPA.

XRD is one of the best techniques to characterize the effect of the preparation method on the crystalline biochar phase. The XRD patterns of samples are shown in Figure 4a. The RBC and HBC had broad and weak diffraction peaks at 2θ = 25.8° and 42.8°, corresponding to the graphite (002) and (100) crystal face diffraction of amorphous carbon [28–31]. The intensity of the carbon peak gradually strengthened for FMBC (compared with RBC) after being added to $FeCl_3$ and $Mg(NO_3)_2$. This confirmed that the addition of metal salts formed a large and orderly crystal structure. CBC had a more intense carbon peak than FMBC, which was attributed to FeO being continuously oxidized to Fe_3O_4 by H_2O (g), making the reaction between carbon and Fe_3O_4 continue. At the same time, it increased the degree of graphitization and the thermal conductivity of biochar and sped up the CO_2 adsorption and desorption processes of biochar. The XRD peak intensity of carbon weakened for CBC-50-TEPA (compared with CBC). This indicated TEPA was impregnated into the pores of CBC. In addition, TEPA impregnation induced a structure in which the edges or sides of a stacked, layered, and connected structure were destroyed so that the XRD pattern peak intensity weakened [30]. After TEPA incorporation, there was a bulging peak in front of the (002) crystal face peak, and the half peak width widened. This confirmed that the amine impregnation prevented the restacking of a part of the CBC's lamellar structure [31].

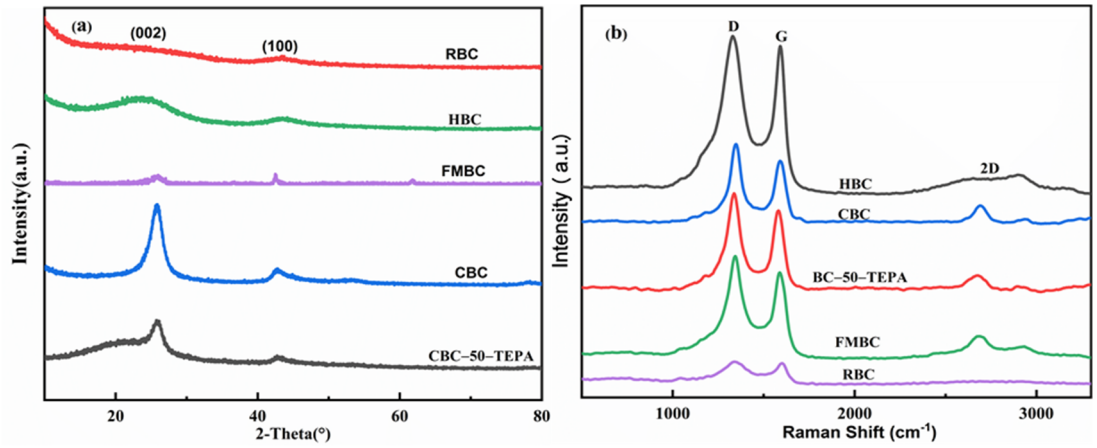


Figure 4. XRD spectra (**a**), Raman spectra of biochar from different activation methods, and CBC-50-TEPA (**b**).

Figure 4b shows the Raman spectra of the samples. The RBC had a weak G peak at 1570 cm^{-1}, a D peak at 1340 cm^{-1}, and no 2D peaks at 2670 cm^{-1}. The HBC had intensity G and D peaks. However, the 2D peak weakened. FMBC had high-intensity D and G peaks and a 2D peak. CBC spectra had both high-intensity G and D peaks and weak 2D peaks. The symmetrical stretching vibration of the sp^2 carbon atom in the aromatic ring produced the D peak, which represents the purity and defects of the graphite structure [32]. The tensile vibration between the carbon atoms of sp^2 caused the appearance of the G peak. The double resonance transition of two phonons of carbon atoms with opposite momentum produced 2D peaks, reflecting the number of layers of carbon [33]. The Raman spectra of CBC-50-TEPA were similar to that of the CBC, indicating that the structure was unchanged after TEPA modification, which agreed with SEM results. The ratio of D to G (I_D: I_G) is an essential parameter for investigating carbon graphitization. The I_D: I_G of the RBC, HBC, FMBC, CBC, and CBC-50-TEPA were calculated as 2.62, 2.42, 1.86, 1.65, and 1.46, respectively.

Figure 5a shows adsorption–desorption isotherms of samples. According to the IUPAC classification, hysteresis loops appeared in the adsorption–desorption isotherm so that mesopores were present in all samples. Figure 5b shows that the pores of the CBC were mainly mesopores, primarily distributed between 4 and 20 nm, whereas few were micropores. There were primarily micropores and some mesopores regarding the

RBC, HBC, and FMBC. The TEPA blocked micropores in the adsorbent w, but some large mesopores were retained.

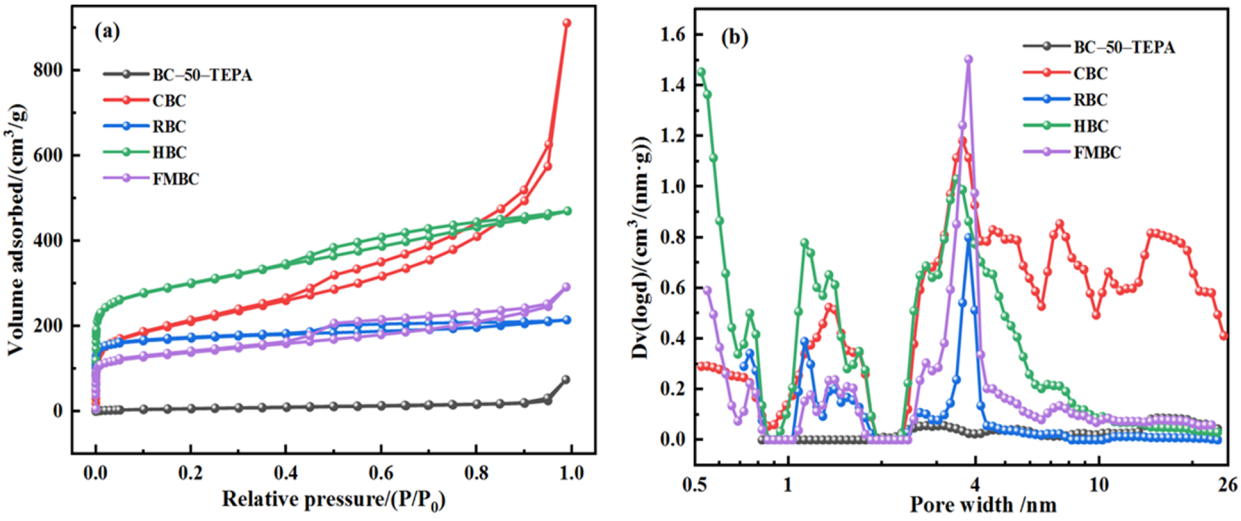


Figure 5. (**a**) Nitrogen adsorption−desorption isotherms and (**b**) pore diameter of biochar from different activation methods and CBC-50-TEPA.

Table 2 lists the specific pore properties of the RBC, HBC, FMBC, CBC, and CBC-50-TEPA. Comparing CBC with other biochars, S_{BET} slightly increased. However, V_T, S_{meso}, and V_{meso} significantly increased, which indicated the high efficiency of combining H_2O (g) with bimetal salts to change the pore structure. According to Sun et al. [34], the pore channels of biochar collapsed at high temperatures, thereby increasing both the V_T and P_d of biochar, whereas the corresponding S_{BET} and the number of pores decreased. However, in this study, while effectively increasing the V_T and P_d of CBC, the S_{BET} was also increased. This was due to the new pores created by metal salts and H_2O (g), and it removed the Fe_3O_4, while MgO particles formed the stacked lamellar structure. The S_{BET} and V_T of CBC had a positive effect on the CO_2 adsorption capacity of the solid amine adsorbent, and the S_{meso} and V_{meso} are more vital than other pores [35]. In addition, compared to the reported results [11–17], when biochar had a large specific surface area, it also had a small pore volume and average pore size. In the process of amine modification, the micropores are easily blocked by organic amine molecules. Therefore, microporous biochar is not suitable for organic amine modification.

Carbon content in CBC was extremely high, whereas the N, H, and O contents were low (Table 3). During pyrolysis, a dehydration reaction reduced the H: C and O: C ratios, and the breakdown of macromolecular organic nutrients into smaller molecules occurred, which spilled over along with volatile fractions and decreased the N content in the CBC at 900 °C [36]. In addition, the N content of CBC-50-TEPA (7.34%) was approximately 28.6 times that of CBC (0.47%), which indicated that a mass of amine was attached to the CBC during functionalization. This further confirmed the effectiveness of TEPA as an ample origin of N (37%) with high amino density. According to the N content of elemental analysis, the actual loading of TEPA was calculated as 35.0% less than 50.0%, which was because, during TEPA immersion, some pores of the CBC were blocked, preventing the amine from continuing to diffuse deeply into the interior. In addition, the O content in the adsorbent increased because of the adsorption of CO_2 and H_2O by the samples.

Table 2. Porous texture properties of biochar from different activation methods and CBC-50-TEPA.

Samples	S_{BET}/ (m^2 g^{-1}) [a]	V_T (cm^3 g^{-1}) [b]	S_{meso}/ (m^2 g^{-1}) [c]	V_{meso} (cm^3 g^{-1}) [d]	D_A/(nm) [e]	Ref.
RBC	667.42	0.33	80.15	0.09	1.98	present work
HBC	998.50	0.73	239.09	0.31	2.91	present work
FMBC	500.18	0.45	206.76	0.31	3.61	present work
CBC	744.38	1.41	425.47	1.23	7.57	present work
CBC-50-TEPA	23.67	0.12	16.44	0.11	19.39	present work
US-MS 700	588	0.21	—	—	—	Chatterjee et al. [11]
Steam AC	840	0.55	—	—	3.77	Sepideh et al. [12]
CHC-O6S20	333.81	0.15	—	—	3.77	Fu et al. [22]
H_3PO_4-81.21	1725.7	1.54	—	1.53	3.72	Villota et al. [14]
C-Na_2CO_3	708	0.3	—	—	—	Demir et al. [15]
BCO	25.3	—	—	—	—	Gao et al. [16]
Char-Fe	517.96	0.33	—	—	2.61	Liu et al. [17]

[a] S_{BET} was obtained by the BET method. [b] V_T at $p/p_0 = 0.99$. [c] Mesoporous surface area was acquired by the BJH method. [d] Mesoporous pore volume was acquired by the BJH method. [e] Average pore diameter.

Table 3. Elemental analysis of CBC and CBC-50-TEPA (*wt*%).

Sample	C	H	O	N
CBC	94.509	0.660	0.188	0.469
BC-50-TEPA	71.532	3.893	4.429	7.34

The FTIR spectra of CBC and CBC-50-TEPA are shown in Figure S2. Regarding CBC, the peak at 1585 cm^{-1} was the C=C vibration peak [37,38]. There were no other oxygen- and nitrogen-containing groups, indicating low N and O contents, which agreed with the elemental analysis. After TEPA modification, the stretching vibration peak of primary amine ($-NH_2$) appeared at 3292 cm^{-1}. Peaks at 2821 and 2930 cm^{-1} were CH_2 stretching vibrations, whereas C–N stretching vibrations were observed at 1308 cm^{-1} [39,40]. The newly added N groups in the CBC showed that TEPA was successfully loaded.

Figure 6 shows the CBC and CBC-50-TEPA TG analyses. Figure 6a shows that the CBC had almost no weight loss in the range of 30–500 °C, which is attributed to the organic matter in the biochar having been volatilized and no organic matter left for decomposition at high temperatures. So, the CBC has excellent thermal stability at high temperatures. There are two weight-loss stages in the curve of the CBC-50-TEPA. The results showed that CBC-50-TEPA only lost 4.7% of its weight within 150 °C. Therefore, it is suitable for CO_2 capture in SFG (50–100 °C). The DTG curves of CBC-50-TEPA and CBC are shown in Figure 6b,c. CBC-50-TEPA has two weight-loss peaks through 38–500 °C and has a wide temperature range of weight loss. CBC-50-TEPA weight loss in the range of 38–105 °C is mainly due to CO_2 and H_2O heat volatilization, and weight loss within 105–500 °C is caused by pyrolysis of TEPA. CBC DTG curve has one weight loss peak at 95–103 °C. The excellent heat resistance of the biochar and aminated biochar makes it potentially applicable to CO_2 adsorption in SFG.

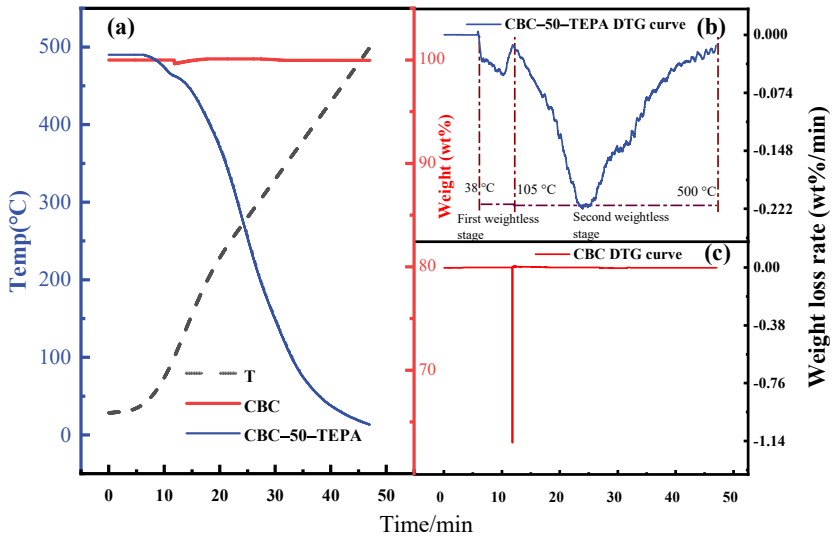


Figure 6. TG curves of weight losses and weight loss rates of pyrolysis and catalytic pyrolysis: (**a**) TGA CBC and CBC-50-TEPA, (**b**) derivative TG (DTG) of CBC-50-TEPA, and (**c**) DTG of CBC.

3.3. CO_2 Adsorption–Desorption

The sorption of CO_2 was performed on a breakthrough adsorption setup. In dry SFG containing 15% CO_2/N_2 85%, the adsorption capacity of CO_2 was tested for CBC-X-TEPA adsorbent (at 101 kPa, 60 °C). Figure 7a,b shows breakthrough adsorption curves and CO_2 adsorption capacities of the adsorbent, which gradually increased as the TEPA loading increased from 20% to 50%; the adsorption time extended, as shown in Figure 7a, and reached a maximum value of 2.82 mmol g^{-1} at 50% TEPA, as shown in Figure 7b. The large pore volume of the CBC provided a large space for the loading of TEPA, which could allow a sufficient amount of amine to penetrate the pore and provide more adsorption sites for CO_2 adsorption.

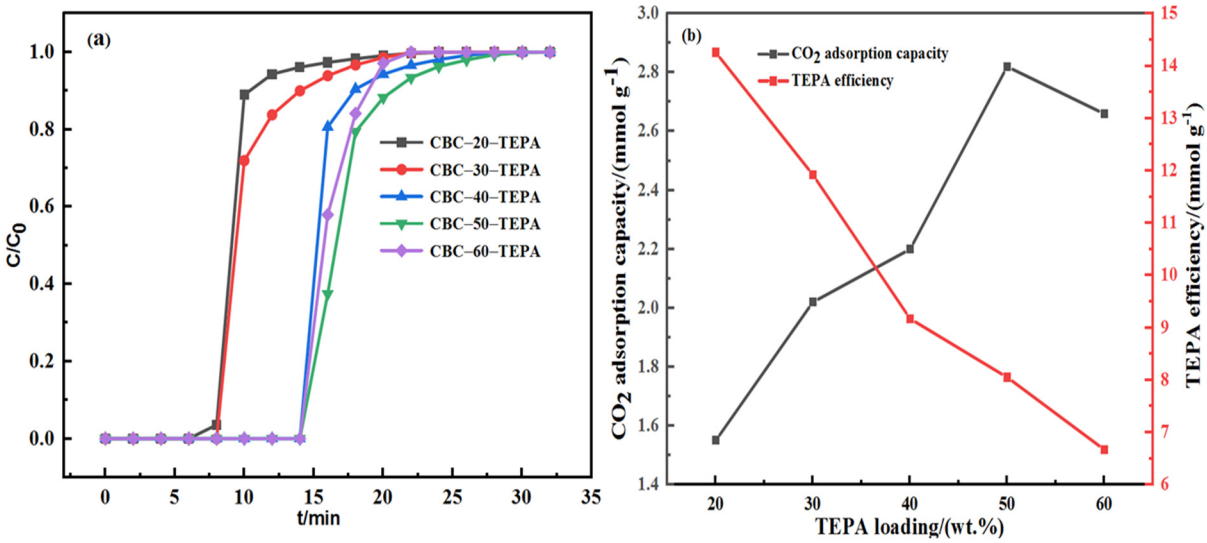


Figure 7. Breakthrough adsorption curves of CO_2 (**a**), and CO_2 adsorption capacity and TEPA efficiencies of CBC-X-TEPA (**b**).

The adsorption capacity started to decrease at 60% TEPA loading, which was because the pores of the adsorbent were blocked so that CO_2 only reacted with the amine-based active sites loaded on the surface of the CBC. In contrast, the organic amines immersed in the pores could not function and reduced CO_2 adsorption capacity. When the amine

efficiency was 8.05 mmol g^{-1}, the adsorption capacity of the adsorbent began to decrease, and the adsorbent reached the optimal load of the amine group.

The adsorption capacity of biochar for CO_2 at 0 °C and 60 °C was also tested. At low temperatures (0 °C, pure CO_2), biochar with high microporosity has a high physical adsorption capacity for CO_2, 4.17 mmol g^{-1}. At 60 °C, the capacity of biochar with high microporosity to adsorb CO_2 is low, only 0.76 mmol g^{-1}, and micropores are no longer the dominant factor for CO_2 adsorption. The results of pore-size analysis showed that the micropores in the biochar after TEPA modification were greatly reduced, and more mesopores and macropores were retained. At 60 °C, the CO_2 adsorption experiment results show that the adsorbent has a high CO_2 adsorption capacity, mainly due to the chemical reaction between the amine group and CO_2, and the adsorption at this time is mainly chemical adsorption. It can be seen that the effect of micropores on chemisorption is not significant. In general, in the adsorption of CO_2 at 60 °C, the adsorbent CBC-50-TEPA was mainly used for chemical adsorption. At the same time, there was also some physical adsorption caused by biochar CBC.

In addition, the adsorption capacity of CBC-50-TEPA was tested using 10% H_2O (g) SFG [15% CO_2/75% N_2/10% H_2O (g)]. The results are shown in Figure 8. Remarkably, it reached 3.31 mmol g^{-1}, 0.49 mmol g^{-1} higher than in the dry SFG, as shown in Figure 8a. TEPA efficiency increased from 8.05 to 9.4 mmol g^{-1}, as shown in Figure 8b, since the presence of H_2O (g) changed the reaction mechanism of the amine with CO_2. The reactions of the amino group with CO_2 in the dry SFG are shown in Equations (16)–(18). When one CO_2 molecule was consumed, two amino functional groups were also consumed [41,42]. In the 10% H_2O (g) SFG, the reactions of the amino group with CO_2 are shown in Equations (19) and (20) [42,43]. One CO_2 molecule was absorbed, and one amino functional group was expended. Therefore, H_2O (g) increased the adsorption efficiency of the amino-functional group and the adsorption capacity of CO_2.

$$2R_1NH_2 + CO_2 \rightarrow \left(R_1NH_3^+\right)\left(R_1NHCOO^-\right) \quad (16)$$

$$2R_1R_2NH_2 + CO_2 \rightarrow \left(R_1R_2NH_3^+\right)\left(R_1R_2NHCOO^-\right) \quad (17)$$

$$R_1NH_2 + R_1R_2NH + CO_2 \rightarrow \left(R_1NH_3^+\right)\left(R_1R_2NHCOO^-\right) \quad (18)$$

$$R_1NH_2 + CO_2 + H_2O \rightarrow \left(R_1NH_3^+\right)\left(HCO_3^-\right) \quad (19)$$

$$R_1R_2NH + CO_2 + H_2O \rightarrow \left(R_1R_2NH_2^+\right)\left(HCO_3^-\right) \quad (20)$$

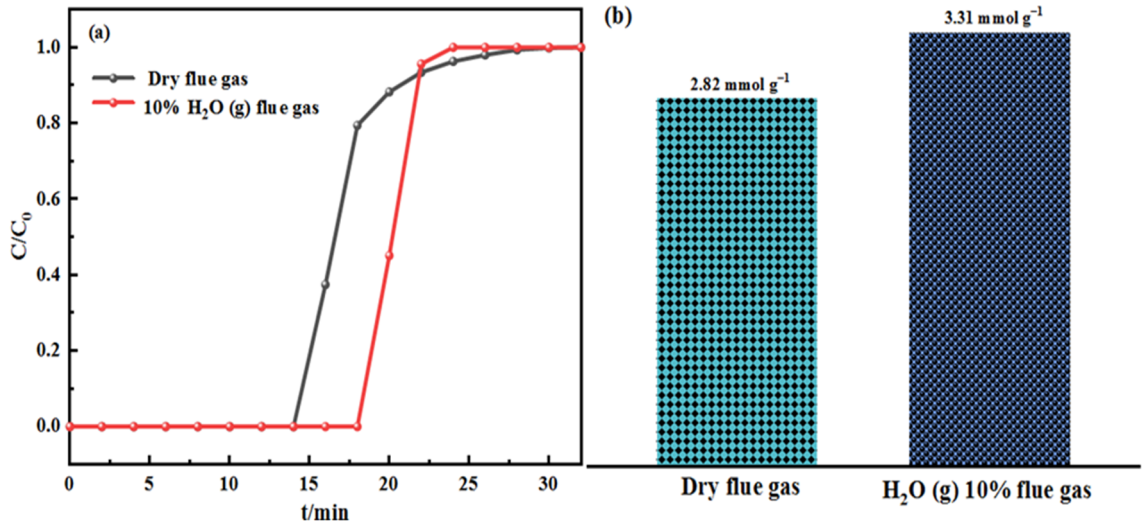


Figure 8. (**a**) Breakthrough adsorption curves and (**b**) adsorption capacity of CBC-50-TEPA in different SFGs.

The CO_2 adsorption capacity of CBC-50-TEPA was compared with those of reported solid amine adsorbents in Table 4. CBC-50-TEPA exhibited an adsorption capacity (3.31 mmol g^{-1}) equivalent to GO (graphene oxide), MCM-41, CNT, and MOFS functionalized by TEPA. This proved that the solid amine adsorbent with biochar as the carrier is also a kind of adsorbent, with potential advantages for removing CO_2 from FG.

Table 4. Comparison of adsorption capacities of CBC-50-TEPA in past research.

Adsorbent	Activating Agent	Temp. °C	CO_2 Partial Pressure (bar)	Adsorption Capacities (mmol g^{-1})	Ref.
CBC	TEPA	60	0.15	3.31	Present work
GO	US-TEPA	70	0.1	1.20	Liu et al. [32]
MCM–41	TEPA	70	0.15	2.45	Wang et al. [5]
MOF	TEPA	60	0.15	2.00	Quan et al. [4]
CNT	PEI	60	0.15	4.75	Wang et al. [44]

3.4. Cyclic Adsorption Experiment

The cycle stability determines the service life of the adsorbent. Figure 9 shows the cycle experiments (adsorption temperature: 60 °C, desorption temperature: 100 °C) of CBC-50-TEPA in the dry and 10% H_2O (g) SFG. The experimental results show that the adsorption capacity of adsorbents decreased from the initial 2.82 to 0.86 mmol g^{-1} after ten cycles in dry SFG. It was not easy to regenerate the adsorption of the product just by changing the temperature. Under dry conditions, amine-group adsorption of CO_2 generated extremely stable adsorption products of urea functional groups [43,45]. Whenever H_2O (g) was present, the adsorption capacity of the adsorbent decreased by only 0.08 mmol g^{-1} from the initial 3.31 after ten cycles, which was almost unchanged. H_2O (g) caused the reaction products between amino groups and CO_2 to be transformed into carbamates [44,46]. It could be effectively regenerated by increasing the temperature, thus keeping the capacity of the adsorbent stable.

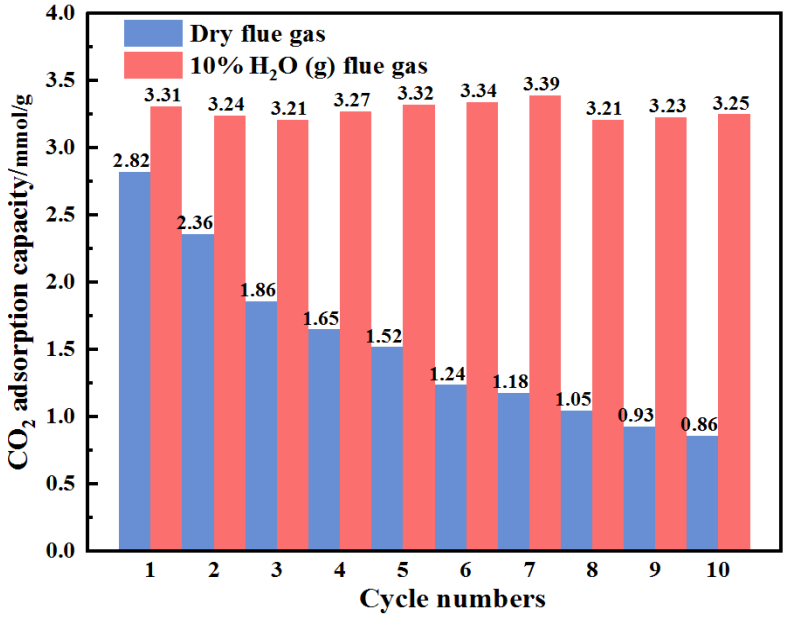


Figure 9. Ten cycles of adsorption capacity of CBC-50-TEPA in different SFGs.

Figure 10 shows the FTIR spectra of the fresh adsorbent and the adsorbent circulating in the 10% H_2O (g) SFG and dry SFG. A new absorption peak appeared at 1658 cm^{-1} after circulating in 10% H_2O (g) SFG, which was the carbonyl peak in urea. Meanwhile, the

N–H and C–H vibration peaks were located at 1570 cm^{-1} and 1460 cm^{-1}, whose intensity weakened compared with the fresh adsorbent [47–49]. However, the adsorbent recycled in dry SFG had a lower peak at 1570 cm^{-1}; the C–H vibration peak at 1460 cm^{-1} almost disappeared. The carbonyl vibration peak at 1658 cm^{-1} was further strengthened. FTIR spectra show that in dry SFG, CBC-50-TEPA formed many urea groups after ten cycles.

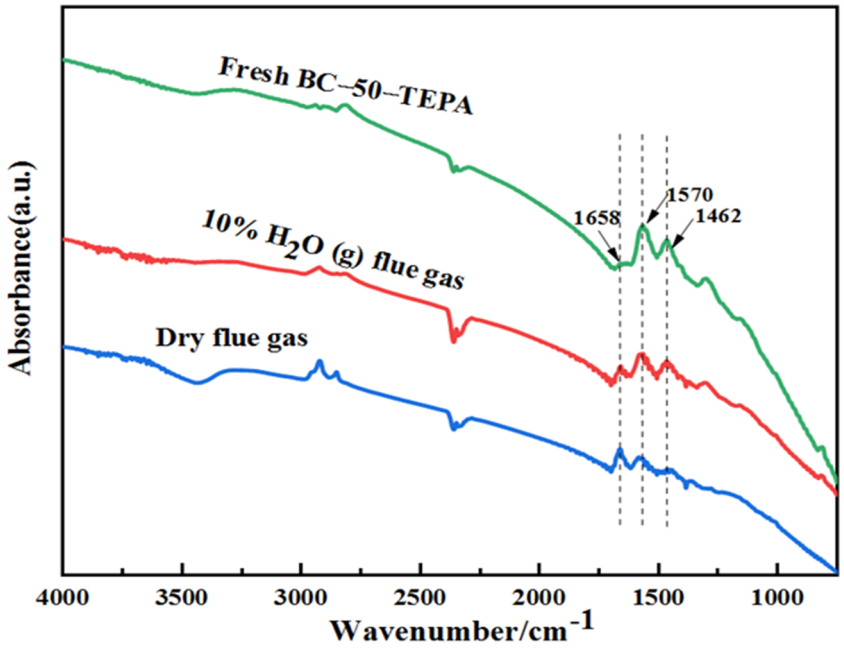


Figure 10. FTIR spectra of the CBC-50-TEPA after 10 cycles in different SFGs.

There are two forms of urea. The open-chain urea is attributed to the dehydration condensation of CO_2 with the different amines in two molecules. The cyclic urea is attributed to the reaction of CO_2 with two amines in the molecules [46,50]. The results indicated that 10% H_2O (g) SFG could delay the CBC-50-TEPA formatted urea, thereby maintaining the stability of the adsorbent.

4. Conclusions

We developed an eco-friendly and cost-effective method to prepare biochar (CBC). At the same time, $FeCl_3$, $Mg(NO_3)_2$, and H_2O (g) activated and increased the ratio of biochar mesopores through a continuous redox reaction. The large V_T (1.41 cm^3 g^{-1}) and S_{BET} (744.38 m^2 g^{-1}) of biochar provided immersion space and channels for the loading of TEPA. The solid amine adsorbent (CBC-50-TEPA) prepared with biochar as a carrier exhibited good thermal stability and a high CO_2 adsorption capacity (3.31 mmol g^{-1}) in 10% H_2O (g) SFG. The H_2O (g) could delay the generation of urea groups, thus allowing the adsorbent to maintain high stability for ten cycles.

Supplementary Materials: The following supporting information can be downloaded at: https://www.mdpi.com/article/10.3390/atmos13040579/s1, Supporting information includes the XRD spectra of metal oxide during the reaction process, the FTIR spectra of the CBC and CBC-50-TEPA, and the formation process of the open-chain and cyclic urea. Figure S1. XRD spectra of Metal oxide during the reaction process, Figure S2. FTIR spectra of the CBC and CBC-50-TEPA.

Author Contributions: W.T.: conceived and designed the research; performed experimental testing; analyzed the data, and wrote the paper. Y.W.: contributed to the design of the experimental scheme and data analysis. J.H.: assisted with manuscript revision. T.G.: assisted with the experimental data analysis and modified the paper. X.W.: assisted with manuscript revision. X.X.: contributed to BET experiment and data analysis. Q.G.: provided constructive suggestions, manuscript revision,

supervision, and funding support. All authors have read and agreed to the published version of the manuscript.

Funding: The Joint Funds of the National Natural Science Foundation of China (grant number U20A20124); the Major Project of the Key Research and Development Program of Ningxia Province, China (grant number 2018BCE01002); The National First-rate Discipline Construction Project of Ningxia (grant number NXYLXK2017A04); The National Natural Science Foundation of China (grant number 22108208); the Foundation of State Key Laboratory of High-efficiency Utilization of Coal and Green Chemical Engineering (grant number 2022–K27).

Institutional Review Board Statement: Not applicable.

Informed Consent Statement: Not applicable.

Data Availability Statement: The data that support the findings of this study are available from the corresponding author, Q.G., upon reasonable request.

Acknowledgments: The authors gratefully acknowledge the financial support from the Joint Funds of the National Natural Science Foundation of China (grant no. U20A20124), the Major Project of the Key Research and Development Program of Ningxia Province, China (2018BCE01002), the National First-rate Discipline Construction Project of Ningxia (NXYLXK2017A04), the National Natural Science Foundation of China (22108208), and the Foundation of State Key Laboratory of High-efficiency Utilization of Coal and Green Chemical Engineering (2022–K27).

Conflicts of Interest: The authors declare no conflict of interest.

References

1. Wang, J.; Song, C.; Yuan, R. CO_2 emissions from electricity generation in China during 1997–2040: The roles of energy transition and thermal power generation efficiency. *Sci. Total Environ.* **2021**, *773*, 145026. [CrossRef]
2. Osman, A.I.; Hefny, M.; Abdel Maksoud, M.I.A.; Elgarahy, A.M.; Rooney, D.W. Recent advances in carbon capture storage and utilisation technologies: A review. *Environ. Chem. Lett.* **2021**, *19*, 797–849. [CrossRef]
3. Yang, Z.X.; Guo, X.F.; Zhang, G.J.; Xu, Y. One–pot synthesis of high N–doped porous carbons derived from a N–rich oil palm biomass residue in low temperature for CO_2 capture. *Int. J. Energy Res.* **2020**, *44*, 4875–4887. [CrossRef]
4. Quan, C.; Su, R.R.; Gao, N.B. Preparation of activated biomass carbon from pine sawdust for supercapacitor and CO_2 capture. *Int. J. Energy Res.* **2020**, *44*, 4335–4351. [CrossRef]
5. Wang, X.; Chen, L.L.; Guo, Q.J. Development of hybrid amine–functionalized MCM–41 sorbents for CO_2 capture. *Chem. Eng. J.* **2015**, *260*, 573–581. [CrossRef]
6. Yang, L.Z.; Yan, L.T.; Wang, Y.; Liu, Z.; He, J.X.; Fu, Q.J.; Liu, D.D.; Gu, X.; Dai, P.C.; Li, L.J.; et al. Adsorption Site Selective Occupation Strategy within a Metal-Organic Framework for Highly Efficient Sieving Acetylene from Carbon Dioxide. *Angew. Chem. Int. Ed.* **2021**, *60*, 4570–4574. [CrossRef]
7. Sharma, H.; Dhir, A. Capture of carbon dioxide using solid carbonaceous and non–carbonaceous adsorbents: A review. *Environ. Chem. Lett.* **2021**, *19*, 851–873. [CrossRef]
8. Qi, Y.F.; Hu, X.D.; Liu, Y.Z.; Sun, D.S.; Li, R.H.; Zhu, H.T. Highly efficient and reversible absorption of SO_2 by hydroxyl ammonium ionic liquids at low partial pressure. *J. Chem. Technol. Biotechnol.* **2019**, *94*, 3325–3332. [CrossRef]
9. Dissanayake, P.D.; You, S.; Igalavithana, A.D.; Xia, Y.; Bhatnagar, A.; Gupta, S.; Kua, H.W.; Kim, S.; Kwon, J.; Tsang, D.C.W.; et al. Biochar–based adsorbents for carbon dioxide capture: A critical review. *Renew. Sustain. Energy Rev.* **2020**, *119*, 109582. [CrossRef]
10. Yuan, T.; He, W.J.; Yin, G.J.; Xu, S.A. Comparison of bio–chars formation derived from fast and slow pyrolysis of walnut shell. *Fuel* **2020**, *261*, 116450. [CrossRef]
11. Chatterjee, R.; Sajjadi, B.; Chen, W.; Mattern, D.L.; Hammer, N.; Raman, V.; Dorris, A. Effect of Pyrolysis Temperature on PhysicoChemical Properties and Acoustic–Based Amination of Biochar for Efficient CO_2 Adsorption. *Front. Energy Res.* **2020**, *218*, 741–748. [CrossRef]
12. Shahkarami, S.; Azargohar, R.; Dalai, A.K.; Soltan, J. Breakthrough CO_2 adsorption in bio-based activated carbons. *J. Environ. Sci.* **2015**, *34*, 68–76. [CrossRef] [PubMed]
13. Idrees, M.; Rangari, V.; Jeelani, S. Sustainable packaging waste-derived activated carbon for carbon dioxide capture. *J. CO_2 Util.* **2018**, *26*, 380–387. [CrossRef]
14. Villota, E.M.; Lei, H.W.; Qian, M.; Yang, Z.X.; Villota, S.M.A.; Zhang, Y.Y.; Yadavalli, G. Optimizing Microwave-Assisted Pyrolysis of Phosphoric Acid-Activated Biomass: Impact of Concentration on Heating Rate and Carbonization Time. *ACS Sustain. Chem. Eng.* **2018**, *6*, 1318–1326. [CrossRef]
15. Demir, M.; Doguscu, M. Preparation of Porous Carbons Using NaOH, K_2CO_3, Na_2CO_3 and $Na_2S_2O_3$ Activating Agents and Their Supercapacitor Application: A Comparative Study. *Chemistryselect* **2022**, *7*, 1–9. [CrossRef]

16. Gao, B.; Wang, Y.; Huang, L.; Liu, S.M. Study on the performance of HNO3-modified biochar for enhanced medium temperature anaerobic digestion of food waste. *Waste Manag.* **2021**, *135*, 338–346. [CrossRef] [PubMed]
17. Liu, S.S.; Wu, G.; Syed-Hassan, S.S.A.; Li, B.; Hu, X.; Zhou, J.B.; Huang, Y.; Zhang, S.; Zhang, H. Catalytic pyrolysis of pine wood over char-supported Fe: Bio-oil upgrading and catalyst regeneration by CO_2/H_2O. *Fuel* **2022**, *307*, 121778. [CrossRef]
18. Yan, L.L.; Liu, Y.; Zhang, Y.D.; Liu, S.; Wang, C.X.; Chen, W.T.; Liu, C.; Chen, Z.L.; Zhang, Y. $ZnCl_2$ modified biochar derived from aerobic granular sludge for developed microporosity and enhanced adsorption to tetracycline. *Bioresour. Technol.* **2020**, *297*, 122381. [CrossRef] [PubMed]
19. Liu, W.J.; Tian, K.; He, Y.R.; Jiang, H.; Yu, H.Q. High–Yield Harvest of Nanofibers/Mesoporous Carbon Composite by Pyrolysis of Waste Biomass and Its Application for High Durability Electrochemical Energy Storage. *Environ. Sci. Technol.* **2014**, *48*, 13951–13959. [CrossRef]
20. Chen, S.S.; Cao, Y.; Tsang, D.C.W.; Tessonnier, J.P.; Shang, J.; Hou, D.Y.; Shen, Z.T.; Zhang, S.C.; Ok, Y.S.; Wu, K.C.W. Effective Dispersion of MgO Nanostructure on Biochar Support as a Basic Catalyst for Glucose Isomerization. *ACS Sustain. Chem. Eng.* **2020**, *8*, 6990–7001. [CrossRef]
21. Diedhiou, A.; Ndiaye, L.; Bensakhria, A.; Sock, O. Thermochemical conversion of cashew nut shells, palm nut shells and peanut shells char with CO_2 and/or steam to aliment a clay brick firing unit. *Renew. Energy* **2019**, *142*, 581–590. [CrossRef]
22. Fu, J.P.; Zhang, J.R.; Jin, C.J.; Wang, Z.Q.; Wang, T.; Cheng, X.X.; Ma, C.Y. Effects of temperature, oxygen and steam on pore structure characteristics of coconut husk activated carbon powders prepared by one–step rapid pyrolysis activation process. *Bioresour. Technol.* **2020**, *310*, 123413. [CrossRef] [PubMed]
23. Feng, D.D.; Zhang, Y.; Zhao, Y.J.; Sun, S.Z.; Wu, J.Q.; Tan, H.P. Mechanism of in–situ dynamic catalysis and selective deactivation of H_2O–activated biochar for biomass tar reforming. *Fuel* **2020**, *279*, 118450. [CrossRef]
24. Lahijani, P.; Mohammadi, M.; Mohamed, A.R. Metal incorporated biochar as a potential adsorbent for high capacity CO_2 capture at ambient condition. *J. CO_2 Util.* **2018**, *26*, 281–293. [CrossRef]
25. Guo, F.Q.; Jiang, X.C.; Li, X.L.; Jia, X.P.; Liang, S.; Qian, L. Synthesis of MgO/Fe_3O_4 nanoparticles embedded activated carbon from biomass for high–efficient adsorption of malachite green. *Mater. Chem. Phys.* **2020**, *240*, 122240. [CrossRef]
26. Jovičić, N.; Antonović, A.; Matin, A.; Antolović, S.; Kalambura, S.; Krička, T. Biomass Valorization of Walnut Shell for Liquefaction Efficiency. *Energies* **2022**, *15*, 495. [CrossRef]
27. Fan, L.S.; Li, F.X.; Ramkumar, S. Utilization of chemical looping strategy in coal gasification processes. *Particuology* **2008**, *6*, 131–142. [CrossRef]
28. Keiluweit, M.; Nico, P.S.; Johnson, M.G.; Kleber, M. Dynamic Molecular Structure of Plant Biomass–Derived Black Carbon (Biochar). *Environ. Sci. Technol.* **2010**, *44*, 1247–1253. [CrossRef] [PubMed]
29. Kim, K.H.; Kim, J.; Cho, T.; Choi, J.W. Influence of pyrolysis temperature on physicochemical properties of biochar obtained from the fast pyrolysis of pitch pine (Pinus rigida). *Bioresour. Technol.* **2012**, *118*, 158–162. [CrossRef] [PubMed]
30. Sui, Z.Y.; Cui, Y.; Zhu, J.H.; Han, B.H. Preparation of Three–Dimensional Graphene Oxide–Polyethylenimine Porous Materials as Dye and Gas Adsorbents. *ACS Appl. Mater. Interfaces* **2013**, *5*, 9172–9179. [CrossRef] [PubMed]
31. Cai, D.Y.; Song, M. Preparation of fully exfoliated graphite oxide nanoplatelets in organic solvents. *J. Mater. Chem. A* **2007**, *17*, 3678. [CrossRef]
32. Liu, Y.M.; Sajjadi, B.; Chen, W.Y.; Chatterjee, R.J. Ultrasound–assisted amine functionalized graphene oxide for enhanced CO_2 adsorption. *Fuel* **2019**, *247*, 10–18. [CrossRef]
33. Tuinstra, F.; Koenig, J.L. Raman Spectrum of Graphite. *J. Chem. Phys.* **1970**, *53*, 1126–1130. [CrossRef]
34. Sun, L.; Tian, C.G.; Wang, L.; Zou, J.L.; Mu, G.; Fu, H.G. Magnetically separable porous graphitic carbon with large surface area as excellent adsorbents for metal ions and dye. *J. Mater. Chem. A* **2011**, *21*, 7232. [CrossRef]
35. Gibson, J.A.A.; Gromov, A.V.; Brandani, S.; Campbell, E.E.B. The effect of pore structure on the CO_2 adsorption efficiency of polyamine impregnated porous carbons. *Microporous Mesoporous Mater.* **2015**, *208*, 129–139. [CrossRef]
36. Guo, Y.; Pan, X.; Zhu, Q.; Ma, J.; Guo, Q. Effect of Biomass-Based Catalyst in Walnut Shell/Polypropylene to BTX. *Fine Chem. Eng.* **2021**, *3*, 11–28. [CrossRef]
37. Alabadi, A.; Razzaque, S.; Yang, Y.; Chen, S.; Tan, B. Highly porous activated carbon materials from carbonized biomass with high CO_2 capturing capacity. *Chem. Eng. J.* **2015**, *281*, 606–612. [CrossRef]
38. Karakaş, C.; Özçimen, D.; İnan, B. Potential use of olive stone biochar as a hydroponic growing medium. *J. Anal. Appl. Pyrol.* **2017**, *125*, 17–23. [CrossRef]
39. Kong, Q.P.; Wei, J.Y.; Hu, Y.; Wei, C.H. Fabrication of terminal amino hyperbranched polymer modified graphene oxide and its prominent adsorption performance towards Cr(VI). *J. Hazard. Mater.* **2019**, *363*, 161–169. [CrossRef]
40. Dao, D.S.; Yamada, H.; Yogo, K. Enhancement of CO_2 Adsorption/Desorption Properties of Solid Sorbents Using Tetraethylenepentamine/Diethanolamine Blends. *ACS Omega* **2020**, *5*, 23533–23541. [CrossRef] [PubMed]
41. Sardo, M.; Afonso, R.; Juźków, J.; Pacheco, M.; Bordonhos, M.; Pinto, M.L.; Gomes, J.R.B.; Mafra, L. Unravelling moisture–induced CO_2 chemisorption mechanisms in amine–modified sorbents at the molecular scale. *J. Mater. Chem. A* **2021**, *9*, 5542–5555. [CrossRef] [PubMed]
42. Wang, Y.X.; Guo, T.; Hu, X.D.; Hao, J.; Guo, Q.J. Mechanism and kinetics of CO_2 adsorption for TEPA- impregnated hierarchical mesoporous carbon in the presence of water vapor. *Powder Technol.* **2020**, *368*, 227–236. [CrossRef]

43. Numaguchi, R.; Fujiki, J.; Yamada, H.; Chowdhury, A.; Kida, K.; Goto, K.; Okumura, T.; Yoshizawa, K.; Yogo, K. Development of Post–combustion CO_2 Capture System Using Amine–impregnated Solid Sorbent. *Energy Procedia* **2017**, *114*, 2304–2312. [CrossRef]
44. Wang, Y.X.; Hu, X.D.; Guo, T.; Tian, W.G.; Hao, J.; Guo, Q.J. The competitive adsorption mechanism of CO_2, H_2O and O_2 on a solid amine adsorbent. *Chem. Eng. J.* **2021**, *416*, 129007. [CrossRef]
45. Choe, J.H.; Kang, D.W.; Kang, M.; Kim, H.; Park, J.R.; Kim, D.W.; Hong, C.S. Revealing an unusual temperature–dependent CO_2 adsorption trend and selective CO_2 uptake over water vapors in a polyamine–appended metal–organic framework. *Mater. Chem. Front.* **2019**, *3*, 2759–2767. [CrossRef]
46. Zhao, X.L.; Cui, Q.; Wang, B.D.; Yan, X.L.; Singh, S.; Zhang, F.; Gao, X.; Li, Y.L. Recent progress of amine modified sorbents for capturing CO_2 from flue gas. *Chin. J. Chem. Eng.* **2018**, *26*, 2292–2302. [CrossRef]
47. Ma, L.; Bai, R.; Hu, G.; Chen, R.; Hu, X.; Dai, W.; Dacosta, H.F.M.; Fan, M. Capturing CO_2 with Amine–Impregnated Titanium Oxides. *Energy Fuels* **2013**, *27*, 5433–5439. [CrossRef]
48. Hladnik, L.; Vicente, F.A.; Novak, U.; Grilc, M.; Likozar, B. Solubility assessment of lignin monomeric compounds and organosolv lignin in deep eutectic solvents using in situ Fourier–transform infrared spectroscopy. *Ind. Crop. Prod.* **2021**, *164*, 113359. [CrossRef]
49. Li, K.M.; Jiang, J.G.; Chen, X.J.; Gao, Y.C.; Yan, F.; Tian, S.C. Research on Urea Linkages Formation of Amine Functional Adsorbents During CO_2 Capture Process: Two Key Factors Analysis, Temperature and Moisture. *J. Phys. Chem. C* **2016**, *120*, 25892–25902. [CrossRef]
50. Zhao, J.; Deng, S.; Zhao, L.; Yuan, X.Z.; Du, Z.Y.; Li, S.J.; Chen, L.J.; Wu, K.L. Understanding the effect of H_2O on CO_2 adsorption capture: Mechanism explanation, quantitative approach and application. *Sustain. Energy Fuels* **2020**, *4*, 5970–5986. [CrossRef]